On the Dynamics of a Storm Track

EDMUND K. M. CHANG

Atmospheric and Oceanic Sciences Program, Princeton University, Princeton, New Jersey

ISIDORO ORLANSKI

Geophysical Fluid Dynamics Laboratory/NOAA, Princeton University, Princeton, New Jersey

(Manuscript received 3 January 1992, in final form 11 June 1992)

ABSTRACT

An idealized primitive equation model is used to determine the factors controlling the dynamics and maintenance of eddy activity in a storm track. The results show that localized regions of enhanced baroclinicity do not necessarily lead to localization of eddy activity. By studying the energetics of the storm track, it is shown that while baroclinic conversion does indeed correlate with the region of maximum baroclinicity, it is the downstream radiation of energy through the ageostrophic geopotential fluxes which acts as a trigger for the development and maintenance of eddy activity over less baroclinic regions, extending the region of eddy activity much further downstream from the region of high baroclinicity. Examples of eddy life cycles are given that show that convergence and divergence of ageostrophic fluxes can dominate baroclinic and barotropic conversion, especially in regions with weak baroclinicity. Factors that may limit the zonal extent of a storm track are discussed. Evidence of downstream development over the wintertime Pacific storm track based on analyses of ECMWF data is also shown.

1. Introduction

The existence of latitudinally and longitudinally confined storm tracks in the Northern Hemisphere winter over the Pacific and Atlantic in the midlatitudes has been well documented [for example, see Blackmon (1976); Lau and Wallace (1979); and more recently Wallace et al. (1988); see also Fig. 13]. Storm frequency maxima occur just downstream of the region of maximum land–sea contrast off the east coast of the continents, where diabatic heating by the warm ocean leads to enhanced baroclinicity in the atmosphere. It seems reasonable to assume that the existence and locations of the storm tracks is somehow related to the existence of these strongly baroclinic regions.

One commonly used measure of the baroclinicity of the atmosphere is the maximum Eady growth rate (Eady 1949; Hoskins and Valdes 1990):

$$\sigma_{BI} = 0.31 f \left| \frac{\partial \mathbf{v}}{\partial z} \right| N^{-1}. \qquad (1.1)$$

Using ECMWF data, Hoskins and Valdes (1990) showed that the location of regions of high baroclinicity over the mean Northern Hemisphere winter conditions correlate very well with regions of high eddy activity. They thus concluded that the time mean flow is consistent with the existence of the storm track. Using a model linearized about the zonal flow, Hoskins and Valdes computed the steady response of the atmosphere to eddy forcing by eddy heat fluxes, eddy momentum fluxes, and diabatic heating. From their experiments, they showed that diabatic heating is essential to the maintenance of the high baroclinicity over the storm track region and thus is essential to the maintenance of the storm track. They further argued that since the diabatic heating over the storm track regions is caused by horizontal and vertical displacements associated with individual storms, the storm tracks can, in that sense, be considered self-maintaining.

If we examine the results of Hoskins and Valdes (1990) closely, we can see that while the regions of maximum diabatic heating are located more or less over the western boundary currents of the oceans, the regions of maximum eddy activity actually are located downstream of those regions and extend quite some distance downstream into regions of lower baroclinicity. While diabatic heating clearly acts to maintain the baroclinicity of the regions directly over the boundary currents, the precise reasons for the downstream extension of the storm track over less baroclinic regions is not completely explained.

The problem of baroclinic instability of zonally varying flows has been studied by Pierrehumbert (1984) using a linear two-layer quasigeostrophic model. From his linear studies, he concluded that for infinite

Corresponding author address: Dr. Isidoro Orlanski, Geophysical Fluid Dynamics Laboratory, P.O. Box 308, Princeton University, Forrestal Campus, Princeton, NJ 08542.

© 1993 American Meteorological Society

channels, localized enhanced baroclinicity will lead to localized modes only if the basic flow is absolutely unstable over some region, while if the basic flow is "convectively" unstable in all regions, it will only have spatially amplifying modes and no localized modes. For periodic channels, the situation is a bit more complex. Pierrehumbert also showed that, in this case, even if the basic state is convectively unstable without being absolutely unstable anywhere, there still exist modes with localized maxima in wave amplitude. However, these modes, which he called global modes, need at least a few global traverse times to become established, and he concluded that these modes are probably unlikely to be important in the real atmosphere. Thus, the question of whether localized baroclinicity in a convectively unstable atmosphere can lead to localized maxima in eddy activity remains unanswered.

The situation only becomes more complex when we consider that atmospheric disturbances are not linear. As Pierrehumbert pointed out, nonlinearity first becomes important near the region of peak amplitude of the linear modes and will limit the growth in those regions first. Hence, any localization will be spread out by nonlinearity. Furthermore, Simmons and Hoskins (1979) and more recently Orlanski and Chang (1993) pointed out that baroclinic waves develop downstream through downstream radiation of energy. Orlanski and Chang showed that downstream radiation of ageostrophic geopotential fluxes by an upstream eddy acts as a trigger for the development of downstream cyclones. This mechanism could lead to the extension of eddy activity in the zonal direction. Thus, it is still not clear what governs the spatial extent of eddy activity in the atmosphere.

In this paper, we will try to gain some insight into what controls the spread of a storm track by studying the dynamics of a model storm track in a zonally varying background flow. The numerical model and experiment design will be summarized in section 2, and the results will be briefly summarized in section 3. The effects of the eddies on the mean flow will be discussed in section 4, and section 5 will examine the spatial distribution of eddy activity in the zonally varying baroclinic flow. In sections 6 and 7, we will study the energetics of individual eddies and of the whole model storm track, respectively. The results will show that downstream development of baroclinic waves is responsible for extending the storm track in the zonal direction. We will discuss in section 8 some factors which may control the zonal extent of a storm track. In section 9, we will look at some evidence of downstream development over the Pacific wintertime storm track. The conclusions are presented in section 10.

2. Experiment description

a. The numerical model

The model used in this study is a simplified version of the gridpoint primitive equation model of Ross and Orlanski (1982). Major simplifications employed here include the neglect of moisture effects, the use of the Boussinesq approximation, and the use of a beta channel instead of full spherical geometry. This version of the model has been described in Orlanski and Chang (1993).

The initial basic state is that of a zonally symmetric baroclinic jet with the following profile:

$$\bar{U} = \begin{cases} 0, & 0 \leq y < \dfrac{L_y - L_B}{2} \\ \Lambda \dfrac{z}{2}\left[1 - \cos\dfrac{2\pi}{L_B}\left(y - \dfrac{L_y - B}{2}\right)\right], & \dfrac{L_y - L_B}{2} \leq y \leq \dfrac{L_y + L_B}{2} \\ 0, & \dfrac{L_y + L_B}{2} < y \leq L_y. \end{cases} \tag{2.1}$$

The basic-state potential temperature is in thermal wind balance with the jet, and the stability is set by fixing the minimum Richardson number of the flow:

$$\mathrm{Ri} = \frac{N_0^2}{\Lambda^2} = \left(\frac{g}{\Theta_0}\frac{\partial\bar{\Theta}}{\partial z}\right)\Big/\Lambda^2, \tag{2.2}$$

(see Fig. 4a for a meridional cross section of the initial state). The model is periodic in the zonal direction. A grid size of 200 km and a channel length of 30 000 km is used for the numerical runs. The width of the channel (L_y) is set to be 10 000 km and the jet width (L_B) is taken to be 6000 km. The vertical resolution is 1 km, f_0 is set to be 10^{-4} s^{-1}, and β is taken to be 1.6×10^{-11} m^{-1} s^{-1}. A fourth-order horizontal diffusion is used to parameterize subgrid-scale dissipation and a diffusion coefficient of 1×10^{16} m^4 s^{-1} is used for the experiments. A Laplacian vertical diffusion with a diffusion coefficient of 5 m^2 s^{-1} is also used.

A simple surface friction of the form

$$\mathbf{F}_s = -k_F(z)|\mathbf{v}_s|\mathbf{v}_s, \tag{2.3}$$

is used in the experiment. This form has been used by Simmons and Hoskins (1978) and is a simple approximation to the bulk aerodynamic stress formulation. The value of k_F is set to be 4×10^{-7} m^{-1} for the lowest level at 500 m, one-third of that value at 1500 m, and zero above. (Although they will not be presented, experiments without surface friction have also been performed and the results are qualitatively similar to those with surface friction except that an unrealistically strong barotropic jet is formed due to the lack of dissipation. We have also performed experiments with stronger friction and obtained qualitatively similar results.)

b. The experimental setup

All of the experiments use a basic-state jet (2.1) with $\Lambda = 0.004$ s^{-1} and a minimum Richardson number of

10, equivalent to a total north–south horizontal temperature difference of about 37°, and a vertical potential temperature gradient of 4° km^{-1}, which is fairly typical of Northern Hemisphere winter conditions. The integration starts with a zonally symmetric jet without eddies.

One of the goals of this study is to investigate the eddy response to zonally changing baroclinicity, and to determine whether zonally changing baroclinicity will limit the zonal extent of the storm track. In order to introduce a region of enhanced baroclinicity, we introduce a sponge region which is centered around $x = 0$. Inside the sponge, temperature and momentum are restored toward the initial basic state by way of a Newtonian damping. The sponge has a Gaussian shape in the zonal direction, and has a minimum damping time scale of 0.1 day. Thus, eddies are effectively damped out inside the sponge and cannot recycle across $x = 0$, and the result is essentially a downstream experiment for a truncated semi-infinite channel. Perturbations are introduced near the left boundary ($x = 2000$ km, just downstream of the sponge) by a barotropic source of heating, with maximum amplitude of 2° d^{-1}. This forcing is periodic with a period of 5 days, similar to the period of the most unstable normal mode. Eddies that develop downstream of the sponge tend to destroy the baroclinicity of the downstream regions, as expected from normal-mode life cycle experiments and downstream experiments. After some time, we expect the baroclinicity immediately downstream to be much stronger than that in regions further downstream.

The existence of the sponge necessitates, of course, the constant input of small perturbations at or near the inflow boundary in order to excite unstable eddies in the interior of the domain. We have tried various different forcings, and found that the results obtained are not affected by either the form, the periodicity, or the amplitude of the forcing, except that the storm track (shown in Fig. 6) is shifted to the right when we use weaker forcing. We believe that the exact form of the forcing does not affect the conclusions of this study.

The experiment was integrated for a total of 200 days, starting from the basic flow without any perturbations. In the next section, we will briefly describe the results of the experiment, and a more detailed analysis will be presented in sections 4–7.

3. Brief description of experiment results

Snapshots of the temperature and pressure at the lowest level (500 m) and the pressure at the uppermost level (9.5 km) on day 50 of the integration are shown in Fig. 1. With a source of heating on the left side of the channel, we can see that disturbances develop over the region and continue to amplify while being advected downstream by the background westerly flow, with eddies extending all the way to the right side of the channel. Even though the channel is periodic, the existence of the sponge around $x = 0$ ensures that no disturbances pass through the region. All eddies are essentially dissipated at the far right of the channel.

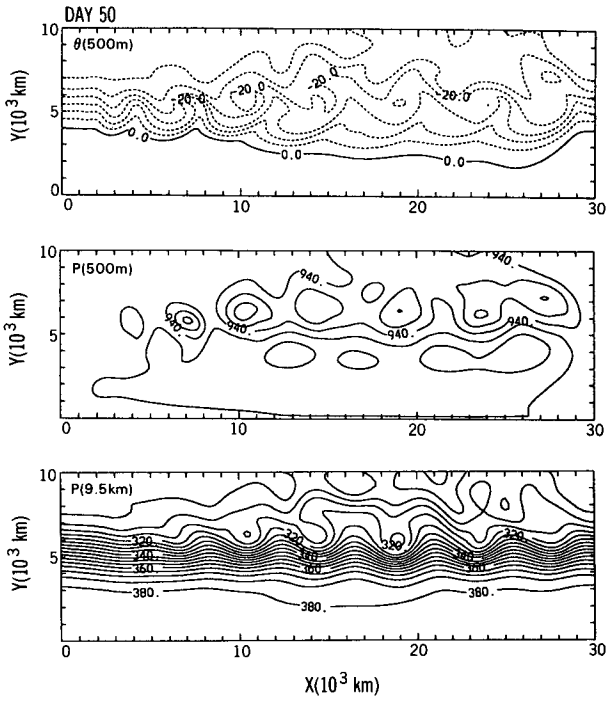

FIG. 1. Horizontal distributions of potential temperature at the lowest model level (500 m), pressure at the lowest model level, and pressure at the highest model level (9.5 km), taken on day 50 of the model run. The contour intervals are 5°C for temperature, and 5 mb for pressure.

Previous studies of the life cycle of baroclinic waves have shown that nonlinear feedback by the eddies on the mean flow will tend to reduce the instability of the mean flow by reducing the horizontal temperature gradient and increasing the vertical stability of the mean state (e.g., see Simmons and Hoskins 1978, 1980; Gall et al. 1979). Figure 1 shows clearly that the eddies do reduce the horizontal gradients over the right half of the channel. However, the temperature gradient is still relatively strong over the left half of the channel immediately downstream of the sponge, since in this region eddies are relatively weak. Hence there is a relative maximum of baroclinicity over the left half of the channel, with baroclinicity decreasing downstream (toward the right). We will return to this point in section 4.

The evolution of the solution is illustrated in Fig. 2, which shows a Hovmöller diagram of the vertical mean eddy kinetic energy at the central latitude of the channel. The vertical axis is time in days, and the horizontal axis is distance in the zonal direction. Here, the eddies are defined by using a simple "high-pass" 24-h difference filter used by Wallace et al. (1988) [see Wallace et al. (1988) for details]. From Fig. 2, we see that eddies

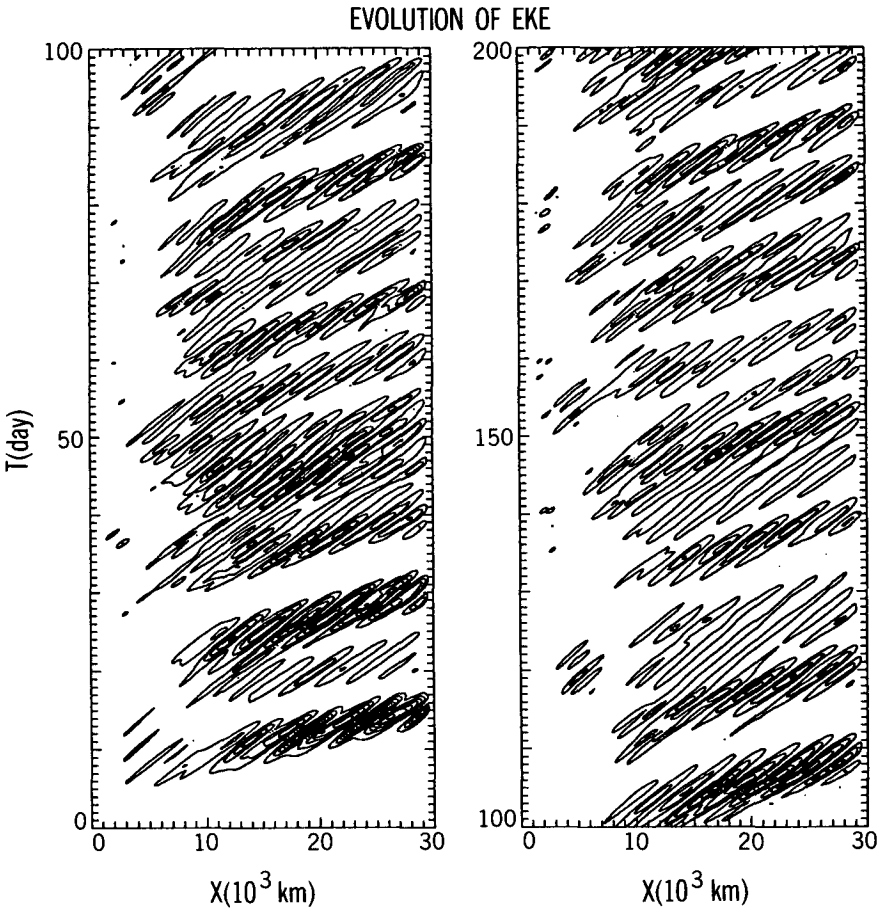

FIG. 2. Hovmöller diagram showing the evolution of eddy kinetic energy for day 1 to day 200. The vertical axis denotes time in days, and the horizontal axis is zonal distance along the central latitude of the channel.

begin appearing after a few days on the left side of the channel, near the region where the heating is applied. Individual eddies can be seen to move downstream with a phase speed of about 11 ms^{-1}, and have a wavelength of about 3900 km. According to the theory of spatial instability (e.g., Pierrehumbert 1984, Merkine 1977), the dominant perturbations observed should have wavelengths and phase speeds equal to that of the most unstable normal mode of the flow. For the basic state given by (2.1), the most unstable normal mode has a wavelength of about 4000 km (see also Fig. 5), and a phase speed of about 13 m s^{-1}, which are very similar to the values estimated from Fig. 2. The individual eddies can be seen to have a definite life cycle of growth and decay as they move downstream. In contrast to the stabilization of the right side of the channel noted previously, there appears to be little difference in the amplitudes of the eddies over the length of the channel.

In addition to illustrating the life cycles of individual eddies, Fig. 2 also shows that eddies tend to develop in groups, with the first one developing on the left side of the channel, a second one appearing to the right shortly after the first, and subsequent eddies developing further downstream at later times, with the whole group propagating downstream as a coherent wave packet. Lee (1991) also found coherent wave packets existing in both idealized models and in observations, and discussed the dynamics of nonlinear wave packets in detail. Such behavior is a characteristic signature of the downstream development of baroclinic waves. Orlanski and Katzfey (1991) and Orlanski and Chang (1993) have shown that the life cycle of baroclinic waves in downstream developments could be quite different from the life cycle of normal-mode developments, the latter having been discussed thoroughly by, among others, Simmons and Hoskins (1978, 1980). We found that the life cycle behavior of individual waves has important implications for the dynamics of the storm track in our model, and the life cycles of individual waves will be discussed in greater detail in section 6.

Linear spatial instability theory also predicts that the peak of the wave packet should move downstream at the real group velocity, $d\omega_r/dk$, evaluated at the

most unstable wavenumber. For the basic state given by (2.1), this group velocity can be found to be about 15.5 m s^{-1} using eigenvalue analysis. From Fig. 2, we see that the peaks of the wave groups propagate downstream at an apparent group velocity of about 35 m s^{-1}, much faster than the group velocity predicted by the linear theory. The reason is that our experiment is nonlinear, with each eddy undergoing a nonlinear cycle of growth and decay. With upstream eddies (which appeared first) decaying due to nonlinearity instead of continuing to grow indefinitely as predicted by linear theory, the peak of the wave group will appear to move downstream with a speed much faster than the group velocity predicted from the linear theory. In fact, the apparent group velocity observed in Fig. 2 is equal to the speed at which the *fringes* of a localized wave packet spread out (e.g., Farrell 1982; Pierrehumbert 1986).

4. Effects of eddy activity on the mean flow

Previous life cycle experiments have shown that baroclinic waves in their nonlinear stage tend to reduce the instability of the mean flow, with eddy heat fluxes reducing the horizontal temperature gradient and increasing the vertical stability. This behavior is also evident in the current experiment (see Fig. 1), in which the horizontal temperature gradient over the right half of the channel is substantially reduced after approximately 50 days. In this section, we will examine more thoroughly the feedback of the eddies upon the mean flow.

a. Changes in the mean flow

Figure 3 shows the baroclinicity index [as defined in Eq. (1.1)] computed by using the time mean for days 180 to 200. The vertical gradients are computed using differences between 3.5 km and 1.5 km levels. The maximum value of the initial undisturbed state is about 0.88. Again, we see the maximum in baroclinicity over the left side of the channel just downstream of the sponge, with the baroclinicity decreasing further downstream. Over the right side of the channel, the baroclinicity has been significantly reduced in the middle latitudes, with stronger baroclinicity both to the north and to the south. This is in agreement with previous life cycle studies which showed that the feedback of the eddies on the mean flow tends to produce a rather barotropic jet and reduce the temperature gradients significantly, while increasing the temperature gradients both north and south of the jet.

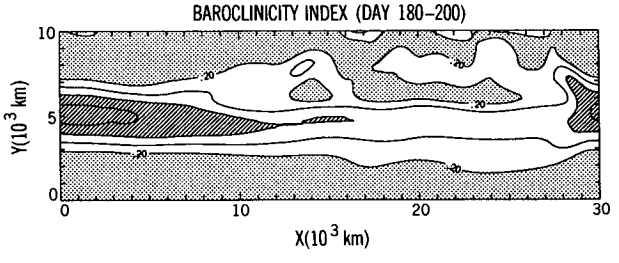

FIG. 3. Baroclinicity index computed using 20-day time mean fields centered on day 190. The shaded regions mask out areas of strong baroclinicity ($\sigma_{BI} > 0.6$ hatched) and weak baroclinicity ($\sigma_{BI} < 0.2$ stippled), respectively. Contour interval is 0.2.

Figure 4 shows the meridional cross sections of temperature and zonal wind for the zonal mean computed for the left third of the channel (just downstream of the sponge) and the right third of the channel (just upstream of the sponge), again using time mean data for days 180 to 200. Roughly speaking, these two cross sections depict the mean conditions experienced by waves within the left and right sides of the channel during the later part of the experiment. (Although we have chosen to show the cross sections using data from days 180 to 200, the mean state for any period of time after day 40 is not significantly different from that shown in Fig. 4.) The initial, unperturbed temperature and zonal wind profiles are shown in Fig. 4a. Comparing the cross sections, we see that the temperature gradients in the lower troposphere over the right third of the channel have indeed been significantly weakened by eddy activity, with the westerly jet becoming much narrower and more barotropic compared to the initial state. On the other hand, since the amplitudes of the eddies are still relatively weak over the left third of the channel, the change in the mean state is relatively minor, even after 200 days. The use of a β plane for our experiment has led to a sharpening of the jet without any northward shift, since the eddy momentum fluxes converge toward the jet axis from both sides (e.g., see Moura and Stone 1976). Other experiments (not shown here) using a sinusoidally varying f clearly show a shift of the jet toward higher latitudes.

b. Growth rates for the modified mean flows

One way to quantify the change in the mean state is by comparing the maximum growth rates of normal modes for the different basic states. A linear version of the model was used to formulate an initial-value problem, and the maximum growth rate of various wavelengths for the three basic states shown in Fig. 4 was computed. The model was initialized with a sinusoidal perturbation in the zonal direction, and integrated until the growth rate reached a constant value, at which time the solution was dominated by the fastest growing normal mode for that wavelength. The maximum growth rates for various wavelengths are shown in Fig. 5. The solid curves show the results without including the effects of surface friction, while the dashed curves show the results including an approximation of the friction by linearizing about the surface mean wind. First let us look at the results without friction. The fastest growing normal mode based on the experiment initial

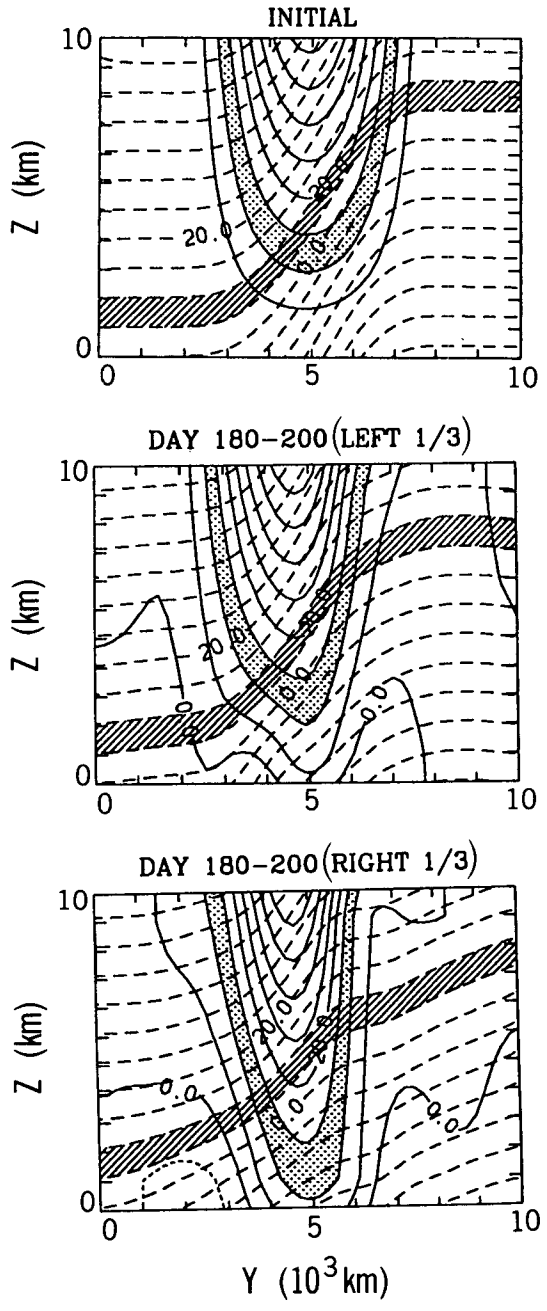

FIG. 4. Meridional cross section of potential temperature (dashed lines, contour interval 5°C) and zonal velocity (zero and positive shown by solid curves, negative values shown by dotted curves, contour interval 5 m s^{-1}): (a) initial undisturbed basic state for all experiments, (b) time and zonal mean flow for the left third of the channel for days 180–200, (c) time and zonal mean flow for the right third of the channel for days 180–200. Zonal winds between 10 and 15 m s^{-1}, and temperatures from 5° to 10°C are shaded to enhance the differences between the three panels.

conditions has a wavelength of approximately 4000 km with a growth rate of around 0.48 day^{-1}. The growth rates based on conditions in the left half of the channel (after 200 days) are somewhat lower, but the maximum growth rate is still around 0.33 day^{-1}. However, for conditions in the right third of the channel, the fastest-growing mode has shifted to shorter wavelengths, and the maximum growth rate has dropped to about 0.15 day^{-1} for waves with wavelengths greater than 2400 km.

Let us now examine the growth rates with the effects of friction included. We see that the growth rates for all three cases are reduced, but the reduction is smallest for the initial basic state. This is because we have approximated the effect of friction by linearizing about the surface mean wind, effectively computing the initial growth rate for infinitesimal perturbations. Inspecting Fig. 4, we see that the surface mean wind is weakest for the initial basic state and is stronger for the two other cases. We expect that as eddies grow, the nonlinear effect of surface friction will further reduce the growth rate [e.g., see Valdes and Hoskins (1988) and references therein]. The maximum growth rates based on the left half of the channel have now dropped to about 0.25 day^{-1}, and those for the right half of the channel have dropped to 0.1 day^{-1} or less.

The principal conclusion from Fig. 5 is that there is a significant change in the instability of the flow along the zonal direction in the channel, with maximum baroclinicity (instability) over the left side of the channel just downstream of the sponge region, and very weak baroclinicity over the right side of the channel. In the next section, we will examine whether this lo-

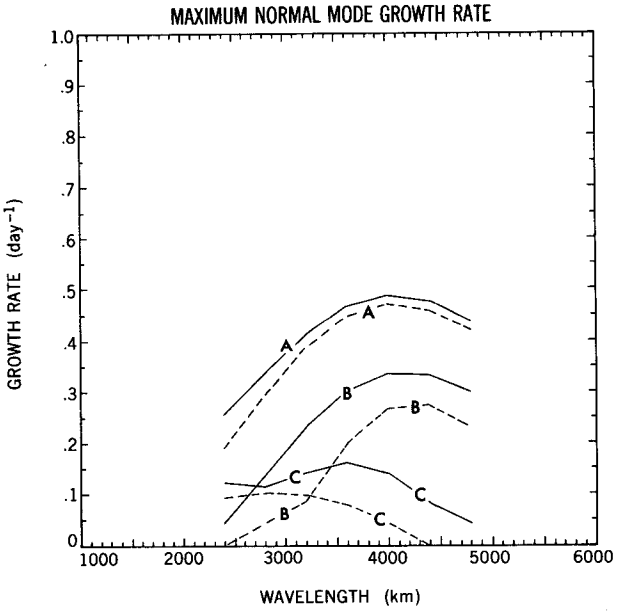

FIG. 5. Maximum linear normal-mode growth rate (day^{-1}) versus wavelength. The three different labels A, B, and C are for the three different meridional cross sections shown in Fig. 4. Solid curves show the growth rates without including the effects of surface friction, while the dashed curves show the results including surface friction linearized about the surface mean wind.

calization of high baroclinicity has any effect on the spatial distribution of eddy activity.

5. Relation between location of maximum baroclinicity and eddy activity

In the previous section, we have seen that the feedback by the eddies on the mean flow creates a mean state which is more unstable over the left part of the channel, and much less unstable over the right part of the channel. In this section, we will examine the spatial distribution of eddies corresponding to such a distribution of baroclinicity.

As discussed in section 1, Pierrehumbert (1984) showed that zonally localized baroclinicity in an infinite channel will not lead to localized normal modes unless the basic state is absolutely unstable in some regions, while "global" modes that have localized amplitude maxima do exist for periodic channels. In the present experiment, the sponge located at $x = 0$ prevents the eddies from being recycled across the sponge region, and our experiment therefore more closely resembles one performed in a truncated semi-infinite channel than one in a periodic channel. Since our basic state is not absolutely unstable, the linear results of Pierrehumbert (1984) suggest that we should observe only spatially amplifying modes in our study.

However, that conclusion is unclear for our nonlinear experiment. The existence of spatially amplifying modes in the linear studies depend on the fact that all eddies will continue to amplify as long as the linear growth rate is greater than zero. If this is so, as an eddy moves downstream, it will continue to grow despite decreasing baroclinicity, giving rise to spatially amplifying modes. If nonlinear effects are included, eddies will interact with and lose energy to the mean flow, leading to the decay of the eddies. Hence in nonlinear studies, all eddies demonstrate a life cycle of growth and decay, as illustrated by the Hovmöller diagram in Fig. 2. In this case, eddies which developed in the strongly baroclinic zone decay before they can move into the weakly baroclinic zone, and eddies that exist deep within the weakly baroclinic zone must have developed entirely over weakly baroclinic zones. That the instability in the weakly baroclinic zones is much smaller opens the question of how eddies can grow, or even be maintained, in those zones. In subsequent sections, we will show that downstream development of baroclinic waves, as discussed in Orlanski and Chang (1993), plays an important role in maintaining the eddies in such regions.

The Hovmöller diagram shown in Fig. 2 indicates that there is no significant change in the strength of the eddies over much of the length of the channel. Figure 6 shows the rms eddy height distribution at the highest model level (9.5 km), computed using the 24-h difference filter, where each panel is composed of data from a 20-day period centered on days 30, 70, 110, 150, and 190. (The vertical coordinate employed by the model used in this study is height rather than pressure, but height variations are directly proportional to pressure variations.) From Fig. 6, we can see the spatial as well as the temporal evolution of eddy activity. The rms eddy height distribution over the entire period between day 40 and day 200 is shown in the last panel. While the strength of the eddies decreased slightly from

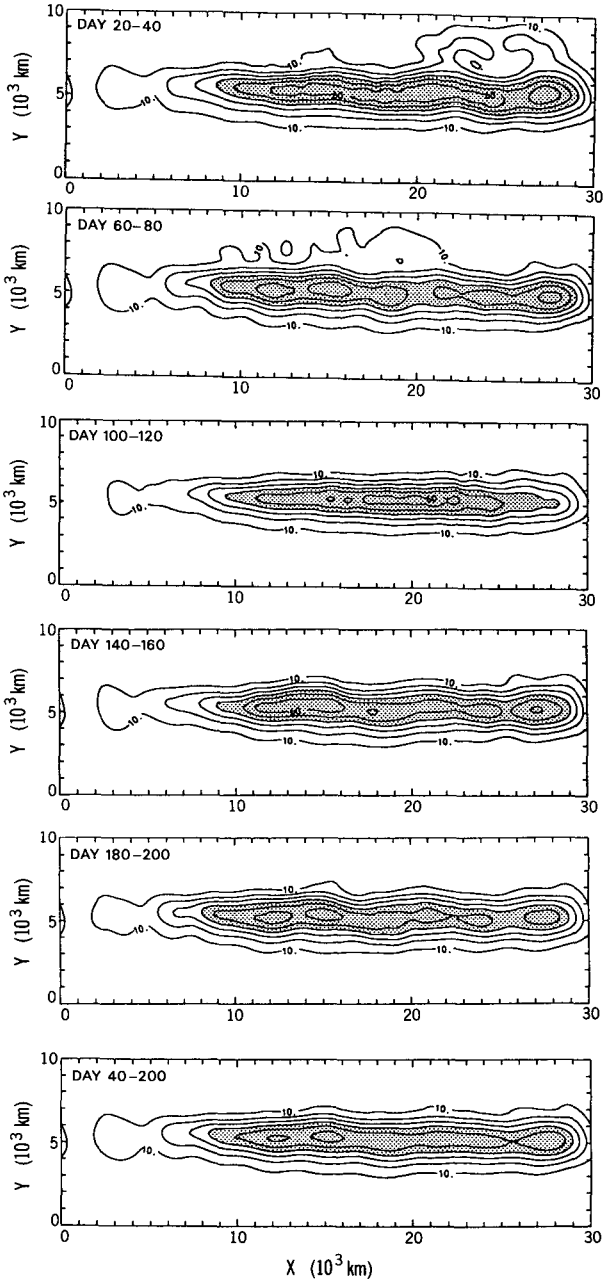

FIG. 6. Rms eddy height distribution at 9.5 km computed using the 24-h difference filter for 20-day periods centered on days 30, 70, 110, 150, and 190. The last panel is for the period from day 40 to day 200. The contour interval is 10 m.

days 20–40 to days 60–80, there was little change after that time, indicating that a statistically steady state was reached after, say, day 60. It is obvious that the eddy activity is confined over the central latitudes of the channel, and this band of eddy activity can be considered to be the "storm track" of our model.

Figure 6 also shows that the eddy activity extends all the way to the right end of the channel. In some of the panels, a weak maximum can be seen over the left half of the channel. However, this maximum is extremely weak, and certainly cannot be said to constitute a localization of eddy activity over the strongly baroclinic region. If we define the length of the storm track by the half-width of eddy activity in the zonal direction, the model storm track in this case has a length in excess of 20 000 km, and hence we can conclude that for this experiment, downstream decrease in baroclinicity does not limit the zonal extension of the storm track.

6. Life cycles of individual eddies inside the storm track

In order to understand how the eddies are maintained in the region of weak baroclinicity, we will, in this section, focus on the kinetic energy budget of eddies within the storm track. The eddy kinetic energy equation is presented and used to compute the budget of eddies in different regions inside the storm track.

a. The energetics equations

Our use of a localized region of forcing to restore the baroclinicity means that our basic state will be zonally asymmetric. We therefore compute the energy budget by defining eddies as deviations from the time mean flow, as opposed to the zonal mean. The derivation of the energy equations is very similar to that in Orlanski and Katzfey (1991), and the details will not be repeated here.

The budget is divided into a time-mean part and an eddy part by partitioning the velocity and temperature as follows:

$$\mathbf{V} = \mathbf{V}_m + \mathbf{v},$$
$$\Theta = \tilde{\theta} + \theta_m + \vartheta. \tag{6.1}$$

Here, the subscript m denotes the time mean, and the script quantities denote deviation from a time mean. Further, $\tilde{\theta}$ denotes the distribution of potential temperature for the state of minimum potential energy (the state of rest) and is thus only a function of z, and the quantities θ_m and ϑ are deviations from that state. In this and the next section, our eddies will be defined as deviation from the time mean, as shown in (6.1). Note that this definition differs from that of the 24-h difference filter used in other sections. However, we will show in section 7 that the results obtained from using these two definitions of eddies are qualitatively similar.

The time-mean kinetic energy, eddy kinetic energy, time-mean potential energy and eddy potential energy are defined as follows:

$$K_m = \frac{1}{2}(U_m^2 + V_m^2); \quad K_e = \frac{1}{2}(u^2 + v^2);$$

$$P_m = \frac{g}{2\Theta_0(d\tilde{\theta}/dz)}\theta_m^2; \quad P_e = \frac{g}{2\Theta_0(d\tilde{\theta}/dz)}\vartheta^2. \tag{6.2}$$

Here, U_m, V_m, and u, v are the horizontal components of the time mean and eddy wind vectors respectively, and the vertical component is dropped from the kinetic energy because of the hydrostatic assumption; Θ_0 is the mean temperature of the reference state.

Let us concentrate on the eddy kinetic energy equation. Using the definitions of (6.1) and (6.2), we can easily obtain an eddy kinetic energy equation:

$$\frac{\partial K_e}{\partial t} + \mathbf{V}_3 \cdot \nabla K_e = -(\nabla \cdot \mathbf{v}_3\varphi) + \frac{g}{\Theta_0} w\vartheta$$
$$- \mathbf{v} \cdot (\mathbf{v}_3 \cdot \nabla \mathbf{V}_m) + \mathbf{v} \cdot \overline{(\mathbf{v}_3 \cdot \nabla \mathbf{v})} + \text{diss.} \tag{6.3}$$

In (6.3), vector quantities with a subscript 3 represent three-dimensional vectors, and those without the subscript refer to the horizontal components only. An overbar denotes an average over time. The terms on the left are the time tendency and advection of eddy kinetic energy ($-$D in Fig. 8 and 10). The first term on the right is the geopotential flux term (A). As pointed out by Orlanski and Katzfey (1991), since the geostrophic geopotential flux $\nu_g\varphi$ is nondivergent, this first term is entirely due to ageostrophic geopotential fluxes. On a related topic, Grotjahn (1984) showed that the ageostrophic fluxes can lead to the cross-isobaric motion of eddies. Cai and Mak (1990) showed that these fluxes can contribute significantly to the local energetics of unstable local modes, leading to a displacement of the maximum eddy perturbation from the region of maximum energy generation. Both of these studies apply to linear perturbations. Orlanski and Katzfey (1991) found that the ageostrophic fluxes contribute significantly to the growth and decay rates in the nonlinear life cycles of individual cyclones.

The second term on the right represents the baroclinic conversion between eddy potential energy and eddy kinetic energy (B). The third and fourth terms can be combined to represent the barotropic conversion between eddy kinetic energy and mean kinetic energy (C). The last term on the right represents dissipation due to surface friction and diffusion. Note that the energy equation is valid only in the "free" region downstream of the sponge, and not valid inside the sponge area itself where additional forcing terms would be required.

b. Energetics of individual eddies

In this subsection, an energy budget is used to examine the life cycles of two individual eddies. In Fig. 7, we show the evolution of the solution from days 180

to 190. The pressure at the uppermost model level (9.5 km) is shown every two days. We will concentrate on the development of the waves inside the boxed areas in the figure. We see that the wave on the left (wave "L") started to deepen on day 180, reached peak amplitude around day 184, and then weakened afterwards. The wave on the right (wave "R") developed a bit later, reaching peak amplitude around day 186, and then weakened. During its development stage, "L" was located on the left side of the channel, whereas wave "R" developed more over the right half of the channel, which was shown in section 4 to be less unstable.

The energy budget for the two waves is computed following the volumes delineated by the boxed areas in Fig. 7. The areas are chosen so that they have the same volume at all times, and are centered over the eddy kinetic energy maxima, extending from one relative energy minimum to another. In this section, the time mean used to define the eddies is taken to be that of the period from day 180 to 200. The time evolution of the volume-averaged eddy kinetic energy for the two waves is shown in the upper panels of Fig. 8. Wave L displays a life cycle of rapid growth during days 180 to 184, reaching peak amplitude on day 184, and then decaying afterwards. Wave R grew until day 187 and then weakened rapidly.

The curves in the lower panels of Fig. 8 show the contributions to the rate of change of eddy kinetic energy (volume-averaged) due to geopotential fluxes (A), baroclinic conversion (B), barotropic conversion (C), and advection (D) [see Eq. (6.3)]. From Fig. 8a, we see that during the time that wave L amplified (days 180 to 184), the term responsible for this growth is the baroclinic conversion term (B). The barotropic contribution (C) is negative at all times, indicating a conversion from eddy kinetic energy to mean kinetic energy. This is to be expected even in a statistically steady state, since the dissipation of the mean jet by surface friction and diffusion must be compensated for by some source of energy in order to maintain the strength of the jet. The weakening of the wave did not begin until the ageostrophic geopotential flux term (A) became strongly negative, indicating dispersion of energy downstream, similar to the case discussed in Orlanski and Katzfey (1991). During the decay stage of the wave, we can see that the ageostrophic geopotential flux term dominated the barotropic term and was the main sink of eddy kinetic energy for the wave. Hence, we can conclude that wave L grew by baroclinic conversion, but decayed due to downstream radiation of energy (via the ageostrophic geopotential fluxes), with barotropic conversion playing only a secondary role.

Next, we turn to the energy budget of wave R, which reached its peak amplitude on day 187 and then weakened. We see that prior to day 186, the term dominating the growth was the ageostrophic geopotential flux term (A), with the baroclinic conversion term (B) becoming significant only after day 186. This result is similar to

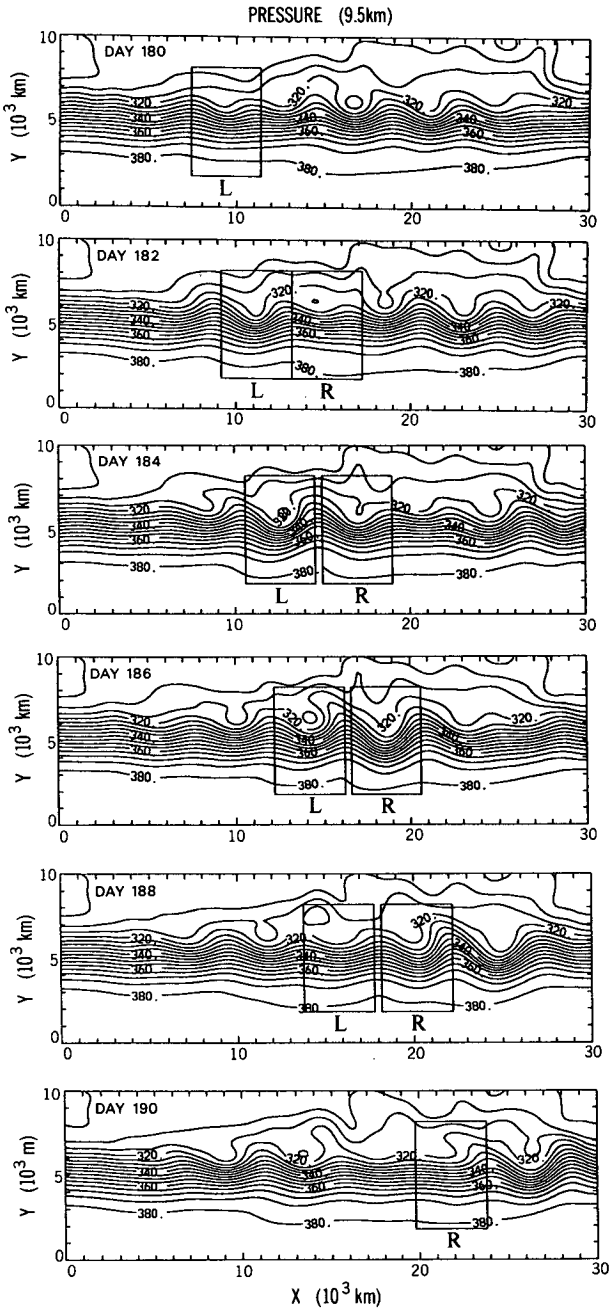

FIG. 7. Evolution of pressure at 9.5 km for days 180 to 190, shown every two days. Contour interval is 5 mb. The boxes in the figure denote the areas for which the volume budget shown in Fig. 8 is computed.

that obtained by Orlanski and Chang (1993) using a similar model. Comparing the energy budget of wave R with that of wave L, we can see that the source of ageostrophic flux convergence fueling the development of wave R from days 182 to 186 was the divergence of fluxes due to radiation of energy from wave L, which led to the decay of wave L. In Fig. 9, the vertically

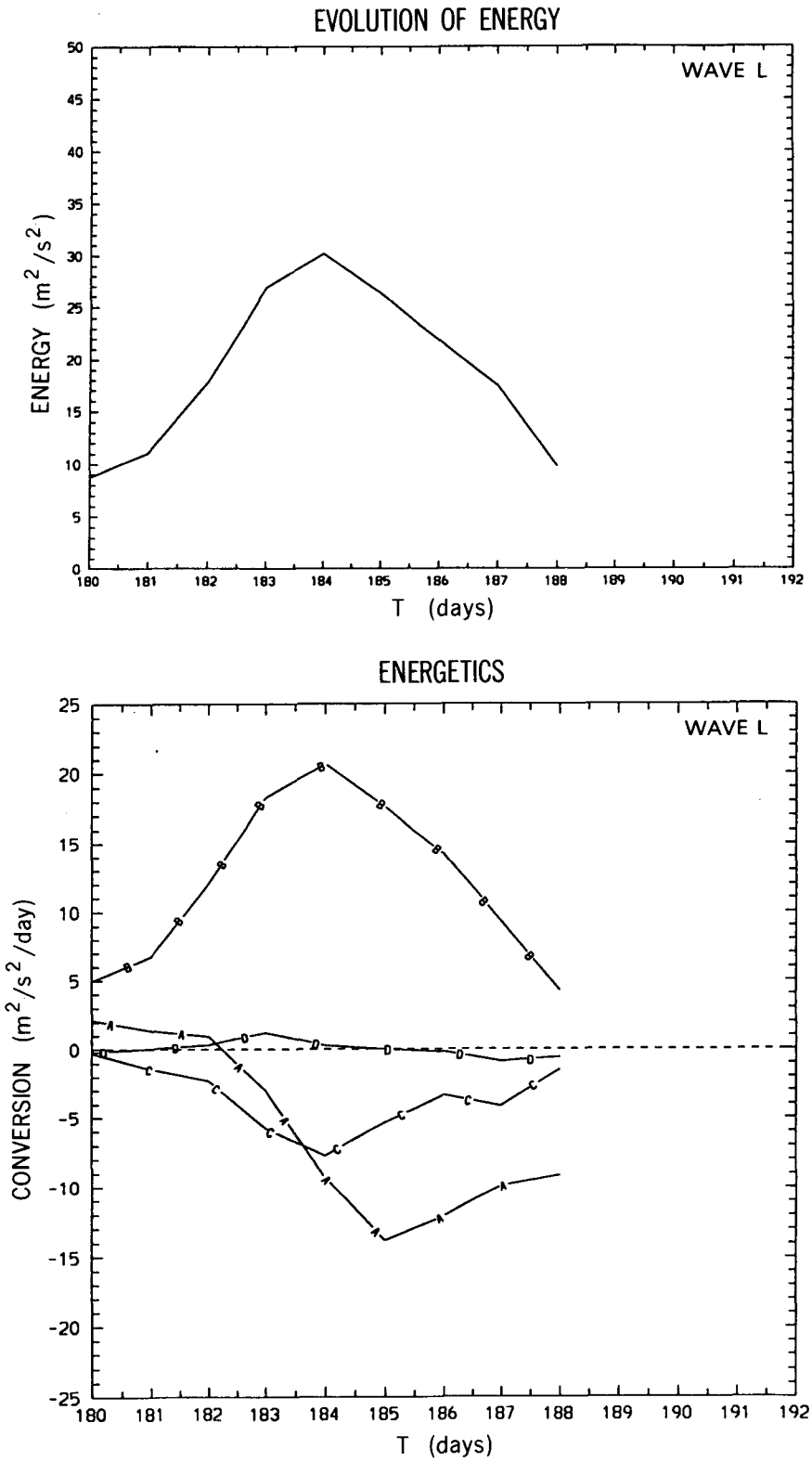

FIG. 8. (a) Upper panel: Evolution of volume mean eddy kinetic energy ($m^2 s^{-2}$) for wave L shown in the boxed area on the left in Fig. 7. Lower panel: Evolution of volume mean eddy kinetic energy budget terms ($m^2 s^{-2} day^{-1}$) for wave L. The curves shown are contributions from the geopotential flux term (A), baroclinic conversion (B), barotropic conversion (C), and advection (D),

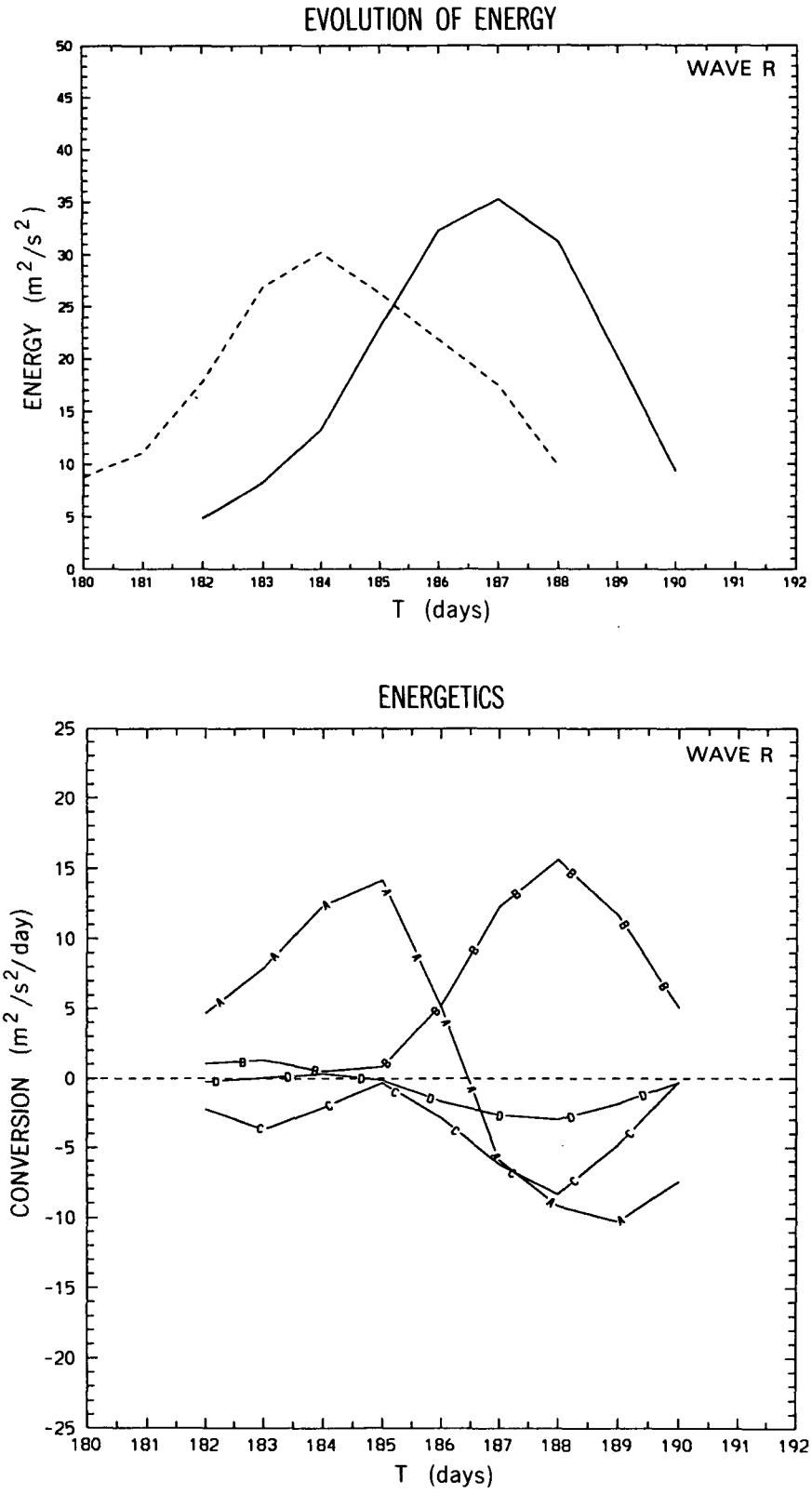

FIG. 8. (*Continued*) respectively, (b) Same as in (a) except quantities are for wave R shown in the boxed area on the right in Fig. 7.

integrated eddy kinetic energy and ageostrophic geopotential flux vectors for three consecutive days (184 to 186) are shown. Notice the radiation of energy from wave L to wave R. Here we clearly see that the radiation of geopotential fluxes from an upstream wave led to the decay of that wave, and became the main source of energy for the development of a new wave downstream. It is clear from Fig. 9 (middle graph, day 185) that wave R is starting to radiate energy downstream, triggering the development of another new wave. We should also note that while on day 188 baroclinic conversion (B) for wave R did increase to a value just slightly less than the maximum for wave L, it did not contribute to the growth of wave R because by that time it was mostly compensated for by the divergence of ageostrophic geopotential fluxes (A) and, in fact, occurred when wave R was already decaying.

In the case of wave R, we see that while the barotropic conversion term (C) is negative all the time, during the decay stage (after day 187), the loss due to divergence of ageostrophic geopotential fluxes is the stronger (more negative) term. Like wave L, the decay of the wave is dominated by divergence of ageostrophic geopotential fluxes. For wave R, we have a life cycle of growth due to convergence of ageostrophic fluxes and decay due to divergence of ageostrophic fluxes, with baroclinic and barotropic conversions playing only secondary roles.

In this section, we have examined the life cycles of two specific waves occurring during the course of the experiment. However, these two waves are not in any way unique. We have examined the energy budget of several other waves, and all of them showed the same pattern of behavior, with waves in the left (more unstable) half of the channel having a life cycle of growth due to baroclinic processes and decay due to divergence of ageostrophic fluxes, and waves over the downstream (more stable) side having a life cycle with both growth and decay dominated by convergence and divergence of ageostrophic geopotential fluxes.

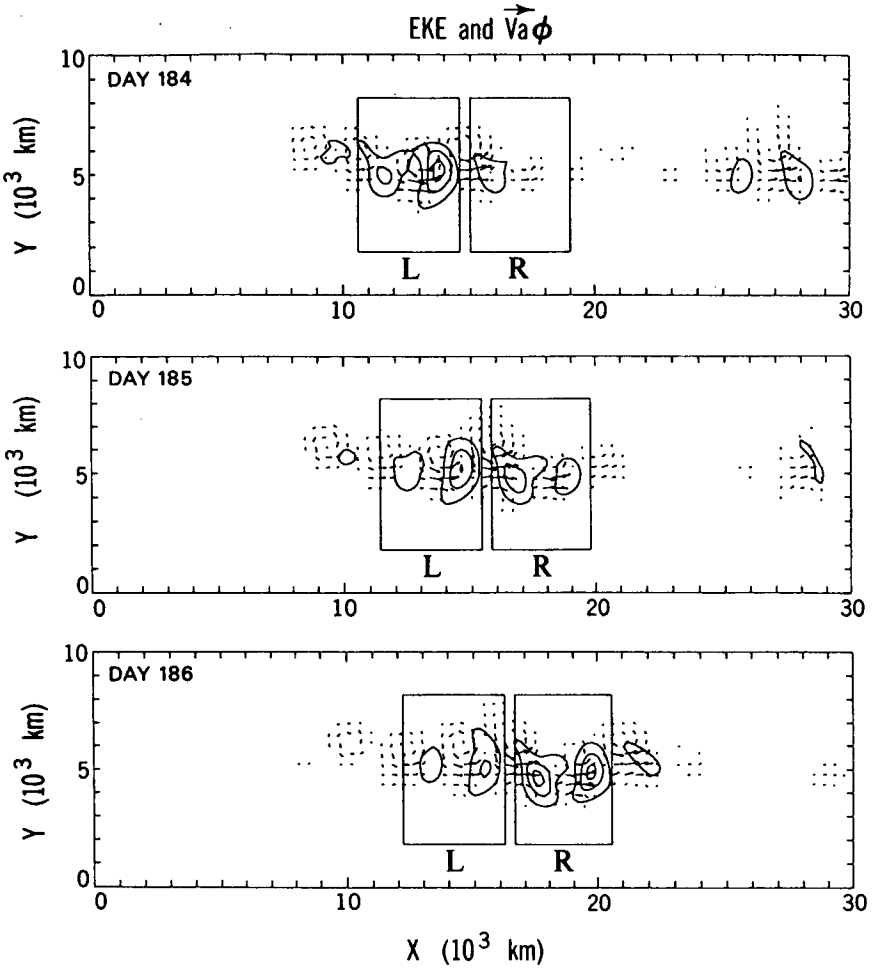

FIG. 9. The contours show the vertically averaged eddy kinetic energy (contour interval 50 $m^2 s^{-2}$), and the vectors show the vertically averaged ageostrophic geopotential fluxes for days 184, 185, and 186.

In section 4, we showed that the mean flow over the right third of the channel is only weakly unstable (with maximum normal-mode growth rate of about 0.1 day^{-1}), which implies that growth due to baroclinic conversion over this region will be weak. We can now begin to understand how the eddies in the weakly unstable right half of the channel are maintained. Waves first develop via baroclinic conversion over the left side of the channel where the flow is rather unstable. As those waves amplify, they radiate energy downstream via ageostrophic geopotential fluxes, and these fluxes act as the source of energy for the growth of the next downstream wave. This next downstream wave in turn will amplify (this time due mainly to convergence of ageostrophic fluxes from upstream), and it, too, starts to radiate energy downstream, causing its own decay but fueling the development of a second downstream wave. As long as the environment is not strongly dissipative (or otherwise strongly unfavorable for growth), this process will repeat itself, leading to the development of more waves downstream and maintaining the eddy activity over weakly baroclinic regions.

One important point to note from the energy budget of wave R (Fig. 8) is that the energy gained by the wave during its growth (days 182 to 186) via convergence of ageostrophic fluxes is roughly equal to the amount of energy it lost due to divergence of ageostrophic fluxes during its decay (days 187 to 190). In a time-averaged budget analysis, ageostrophic flux convergence/divergence will appear to be small, even though it dominates the development of the wave during both the growth and decay stages. We will return to this point in the next section when we discuss the time mean energetics of the model storm track.

7. Energetics of the model storm track

Let us now examine the time-mean energy budget of the entire storm track. Figure 10 shows the time-mean kinetic energy budget computed over days 40 to 200, with each panel showing the contribution to the rate of change of eddy kinetic energy corresponding to each of the terms in (6.3). Here, we do not show the time tendency term, since it is small everywhere and no contours will show up on a plot of the quantity. The quantities shown are the vertical and time mean of the eddy kinetic energy itself, the convergence of ageostrophic geopotential fluxes (A), baroclinic conversion (B), barotropic conversion (C), and advection (D). Dissipation (E) is computed as a residue term.

The storm track, as defined by the eddy kinetic energy, extends all the way to the right end of the channel, with only a very weak maximum over the left half of the channel. (As in the preceding section, we have defined eddies as deviation from the time mean, which is different from the definition of eddies used when referring to the 24-h difference filter.) Note the similarity between the eddy kinetic energy distribution

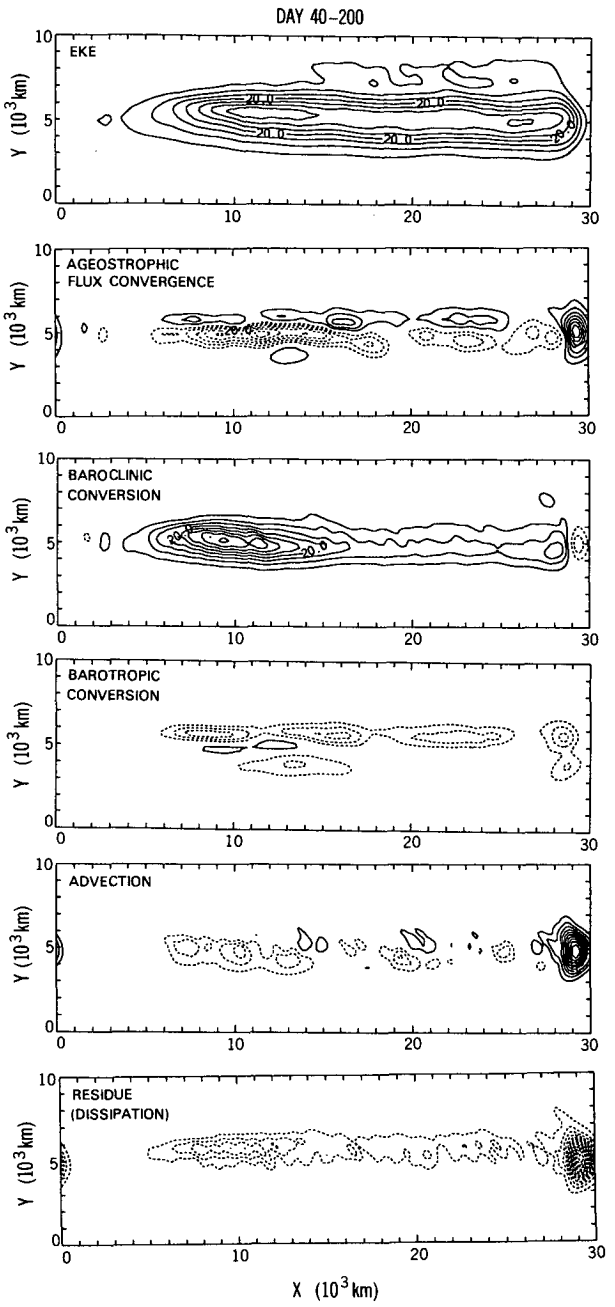

FIG. 10. Kinetic energy budget for days 40–200. Shown in the panels are distribution of (a) the eddy kinetic energy, (b) the geopotential flux term (A), (c) baroclinic conversion (B), (d) barotropic conversion (C), (e) the advection term (D), and (f) the residue (dissipation E). The contour interval is 5 $m^2 s^{-2}$ for (a) and 5 $m^2 s^{-2}$ day^{-1} for (b) through (f).

shown in Fig. 10a with that of the eddy rms height distribution shown in Fig. 6f, indicating that our earlier conclusion that the eddy activity extends far downstream from the region of strong baroclinicity does not depend on how the eddies are defined.

We now examine the contributions from the baro-

clinic conversion term (B). In section 3, we saw that the feedback from the eddies resulted in a mean flow which is much more unstable over the left half of the channel than the right. In Fig. 10, we see that baroclinic conversion is indeed much stronger over the left half of the channel. This is consistent with our findings in section 6 that over the left half of the channel, eddy growth is dominated by baroclinic conversion, whereas over the right half of the channel, baroclinic conversion plays only a secondary role in the life cycle of the eddies.

From Fig. 10, we also see that both barotropic conversion and dissipation are negative over most of the channel, and thus represent sinks of eddy kinetic energy. Over the left half of the channel, we see that ageostrophic geopotential fluxes and advection also act as sinks of eddy kinetic energy, and it is the sum of these four sinks that balances the strong baroclinic source over this rather unstable region. If we look at the magnitudes of these four terms, we see that ageostrophic geopotential fluxes appear to be the strongest sink over the region, as noted in the previous section. Waves over the left half of the channel have life cycles dominated by baroclinic growth followed by decay through downstream radiation of energy via ageostrophic geopotential fluxes.

Over the right half of the channel, we see that all the terms, including the ageostrophic flux term, appear to be rather weak. If we look at the far right side of the channel (inside the sponge), we can see a region of strong dissipation, with strong sources due to advection and ageostrophic fluxes. This indicates that most of the energy radiated downstream from the strongly unstable region over the left half of the channel ended up passing through the entire right half of the channel, to be deposited and dissipated inside the sponge region. Over the right half of the channel, the net contribution from the ageostrophic fluxes in our experiment turns out to be approximately zero. In fact, we see that over this region the weak baroclinic conversion approximately balances the losses due to barotropic conversion and dissipation.

We showed in section 6 that the life cycles of waves over the right half of the channel are dominated by ageostrophic geopotential fluxes both in the growth and decay stages. However, we also showed that the amount of ageostrophic flux convergence (energy gain) experienced by the wave during its growing stage roughly balanced the amount of ageostrophic flux divergence (energy loss) experienced by the wave during its decay stage, hence the near-zero time integral of the ageostrophic fluxes in Fig. 10. Over the right half of the channel, the ageostrophic fluxes dominate the development of individual eddies. The net convergence/divergence in the time-averaged sense is small due to cancellation, but the time-averaged fluxes are very large.

In this experiment, we have a localized region of strong baroclinicity over the left side of the channel and a very weakly unstable region over the right. An analysis of the energetics shows that baroclinic conversion is indeed much stronger over the more unstable region. However, eddy activity occurs not only over this highly baroclinic region, but also extends far downstream to regions that are only weakly unstable. The downstream eddies are maintained by ageostrophic geopotential fluxes radiated downstream from eddies that developed in the more unstable region. This concept is illustrated in Fig. 11. The solid line is the 20 $m^2 s^{-2}$ contour taken from Fig. 10a which, for all intents and purposes, delineates the storm track. The shaded region on the left shows the region of maximum baroclinic conversion (as shown in Fig. 10c), and the hatched region marks out the region of maximum dissipation (taken from Fig. 10f). The vectors show the ageostrophic geopotential fluxes $v_a\varphi$, which extend from the region of maximum baroclinic generation on the upstream end of the storm track all the way downstream to the end of the channel and maintain the eddy activity over the right half of the channel.

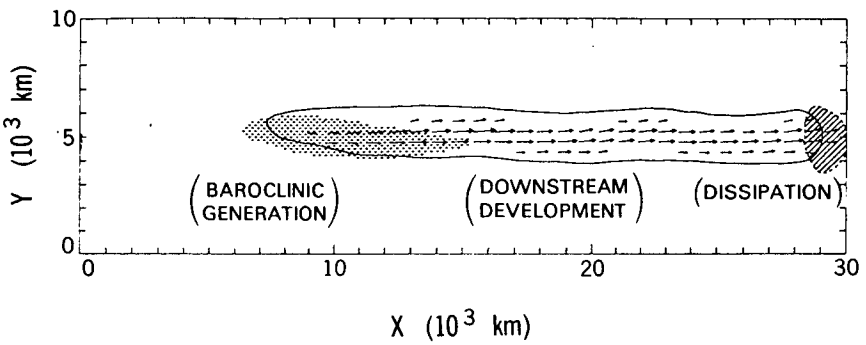

FIG. 11. Solid curve: 20 $m^2 s^{-2}$ eddy kinetic energy contour. Dotted region: baroclinic conversion over +20 $m^2 s^{-2} day^{-1}$. Hatched region: dissipation over −20 $m^2 s^{-2} day^{-1}$. Arrows: ageostrophic geopotential flux vectors. The mean from day 40 to day 200 is shown.

8. Storm track length

In order to demonstrate that the model storm track length is purely a function of the channel length, an additional experiment was run with exactly the same conditions except that the channel length was doubled to 60 000 km. The eddy activity for this experiment, as indicated by the rms eddy height distribution for days 60 to 100, is shown in Fig. 12a. We see that, even for such a long channel, the storm track still extends all the way to the right end of the channel with no significant decrease in strength. In this experiment, the eddies are dissipated by the sponge over the right end of the channel. Even though baroclinic conversion is weak over the right half of the channel, as long as it is strong enough to balance losses due to barotropic decay and dissipation, eddy activity will extend downstream by radiation of energy without decreasing in amplitude. We could imagine cases where an eddy encounters a region of strong dissipation or strong stability such that the baroclinic energy it derives from the mean flow is insufficient to balance the energy it loses through dissipation or barotropic conversion. In that case, it will radiate less energy downstream compared to the amount it receives from its upstream counterpart, and the next downstream eddy will be weaker, leading to a downstream decrease in eddy activity.

To illustrate these ideas, we have also investigated the effects of a zonal change of surface friction by repeating the experiment using the long channel, this time setting surface friction over the right half of the channel to be four times that over the left half of the channel. The form of the surface friction is still defined by (2.3). The integration was started from day 40, using data from the run with uniform surface friction as the initial condition, and continued for another 60 days, up to day 100. Figure 12b shows the rms eddy height variations for the top model level for days 60 to 100. Comparing the results of uniform surface friction shown in Fig. 12a with those of the variable surface friction shown in Fig. 12b, we see a much more pronounced maximum in eddy activity over the left half

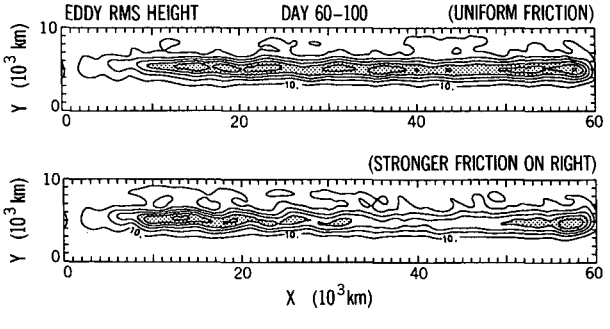

FIG. 12. (a) Rms eddy height distribution at 9.5 km for days 60–100, computed using the 24-h difference filter, for a channel whose length is doubled (60 000 km). (b) Same as in (a) but for a channel with four times stronger surface friction on the right half.

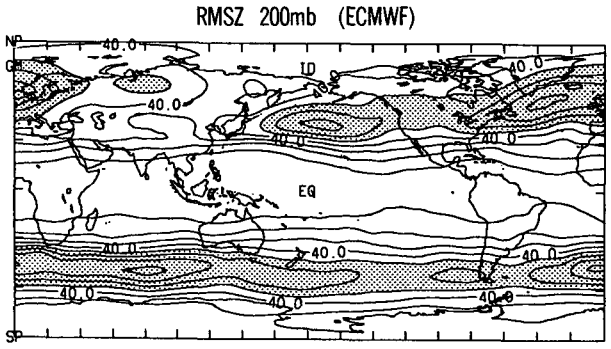

FIG. 13. Rms eddy height distribution at 200 mb for Dec/Jan/Feb from 1980/81 to 1986/87 computed using ECMWF data. The contour interval is 10 m.

of the channel in the latter case, with relatively weaker eddy activity over the right half of the channel. Hence, we can see that a downstream change in surface friction can lead to a zonal change in the eddy activity. In this case, a downstream increase in surface roughness led to a downstream decrease in eddy activity.

Zonal changes in eddy activity are observed in the real atmosphere. Figure 13 shows the rms eddy height distribution at 200 mb computed from ECMWF data for Northern Hemisphere winters (December, January, and February) from 1980–81 to 1986–87. Maxima in eddy activity are evident over the northern Pacific and northern Atlantic. Based on the results of the preceding sections, we expect that these zonal variations of eddy activity cannot be entirely explained by zonal changes in baroclinicity alone. Obviously, in the present idealized study, the whole channel is zonally uniform (apart from the sponge), whereas the real atmosphere possesses substantial zonal variations due to land–sea contrast. The zonally varying distribution of oceans and continents leads to effects due not only to zonal variations in baroclinicity (due to the existence of intense oceanic western boundary currents), but also changes in surface roughness and stationary wave patterns caused by mountains. However, there is an interesting similarity between the observed Southern Hemisphere eddy activity pattern in Fig. 13 and that in the present numerical results shown in Fig. 12a. This similarity may have something to do with the fact that the Southern Hemisphere has minimal zonal variation of surface properties (i.e., mountains, friction) and weaker stationary waves. In this way, the Southern Hemisphere storm track more closely resembles the zonally uniform idealized experiment performed here.

We do not mean to imply that a zonal change in surface roughness is the only thing responsible for the observed zonal changes in eddy activity in Fig. 13. In fact, general circulation model experiments by Manabe and Broccoli (1990) have shown that in GCM runs with land but without topography, the model climatological flow and eddy activity are both much more

zonal than observed, despite zonal variations in surface roughness and diabatic heating. We therefore expect the effects of stationary waves induced by mountains to be important in modulating the eddy activity. Frederiksen (1983) showed, in a linear study, that the existence of ultralong stationary waves in the atmosphere leads to localized unstable modes over the storm track regions. In the light of the results found in this study, it would be interesting to investigate how those modes manifest themselves in fully nonlinear experiments, and how much localization they could produce in the nonlinear situation. Based on the discussions of Pierrehumbert (1984), we expect nonlinearity to reduce the localization indicated by the linear normal modes. Recently, Lee (1991) showed that the existence of stationary waves due solely to the existence of a mountain can modulate the propagation of nonlinear wave packets in weakly baroclinic atmospheres, leading to a maximum in eddy activity just downstream of the mountain. How all these effects interact in the real atmosphere remains to be investigated.

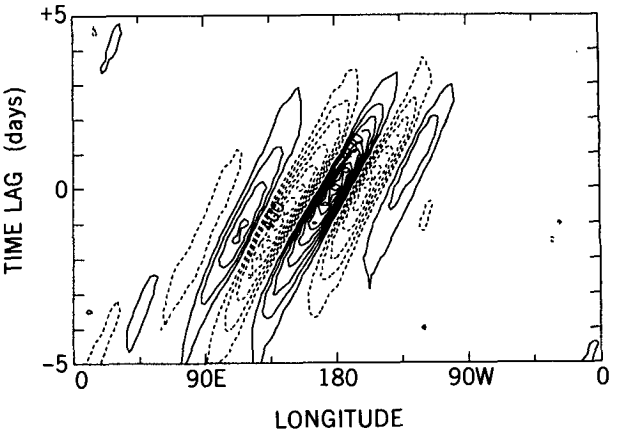

FIG. 14. One point lag–correlation analysis based on ECMWF 300-mb meridional wind data for Northern Hemisphere winters (DJF) from 1980–81 to 1986–87. The data is time-filtered with a 10-day high-pass filter and averaged over the latitude band from 35°N to 45°N. The reference time series is that at 180°E. Contour interval is 0.1, and the zero contour is not shown. Positive values are shown as solid lines, and negative as dotted lines.

9. Observational evidence of downstream development

In sections 6 and 7, we have shown that downstream development of baroclinic waves is the process responsible for the extension of our model storm track into weakly baroclinic regions. The question now is whether this is a pure artifact of our simple model or an important physical process in the real atmosphere as well.

In introducing the use of the "trough-and-ridge" diagram, Hovmöller (1949) showed examples of downstream developing troughs and ridges over the eastern Pacific. More recently, Joung and Hitchman (1982) showed the existence of downstream developing wave trains across the Eurasian continent during East Asian polar air outbreaks. However, recent studies such as Lim and Wallace (1991) did not show any evidence of downstream development of baroclinic waves.

We examined ECMWF data for the winter seasons (December/January/February) of 1980/81–1986/87. The meridional wind component at the 300-mb level is filtered using a high-pass filter with half response at a period of 10 days. The filtered data is then averaged over the latitude band from 35° to 45°N, and time-lagged correlation is computed based on the time series at 180° (the date line). The resulting correlation, after averaging over the seven winter seasons, is shown in Fig. 14. From the figure, the wavelength and phase speed of the wave can be estimated to be about 3900 km and 13 m s^{-1}, which are typical values for synoptic-scale waves (e.g., Blackmon et al. 1984; Lim and Wallace 1991). The main difference between the results shown here and previous similar analyses is in the propagation characteristics of the baroclinic wave trains. In Fig. 14, if we follow the relative maxima in the correlation pattern, we can identify a downstream developing wave train extending all the way from the Eurasian continent toward the west coast of North America across the wintertime Pacific storm track. Similar analyses by Lim and Wallace (1991) and Blackmon et al. (1984) did not find any indication of downstream development. We believe that this difference arises from the use of a different reference variable and different time filters. Here, we show this result only to support the ideas developed in this paper. More details of the data analyses and possible reasons why our results are different from those of Blackmon et al. (1984) and Lim and Wallace (1991) are presented in Chang (1993).

10. Conclusions

The warm ocean currents of the northern Pacific and Atlantic oceans just off the east coast of the continents constitute sources of enhanced baroclinicity over these regions, especially in the winter season. In this paper, an idealized channel model has been used to show that the existence of a localized source of enhanced baroclinicity, while leading to localized maxima in the baroclinicity at, or immediately downstream of, the region, does not necessarily lead to the localization of eddy activity. While baroclinic conversion is indeed a maximum immediately downstream of the source of enhanced baroclinicity, energy radiated downstream by eddies which develop in this region will trigger and sustain eddies in the downstream region, despite the lower baroclinicity there. Hence, the localization of the baroclinic source does not determine completely the spatial extent of the storm track. These results underscore the importance of the ageostrophic geopotential fluxes discussed in Orlanski and Katzfey (1991) and

Orlanski and Chang (1993) and represent the fundamental difference between downstream development and normal-mode life cycles. In section 6, we have shown examples of wave evolution for two waves, one that developed in the upstream, high-baroclinicity region, and the other in the downstream, low-baroclinicity region. For the former, the growth stage was dominated by baroclinic conversions, and decay was due primarily to ageostrophic geopotential fluxes. For the latter, it was found that ageostrophic geopotential fluxes were dominant during both the developing and decaying stages of the wave. In section 9, using ECMWF wind data, we showed indications that downstream development occurs over the wintertime Pacific storm track, suggesting that the process discussed here may indeed be important in the real atmosphere.

In section 8, we have briefly discussed some of the factors which may contribute to limiting the downstream extension of a storm track. We showed that a downstream increase in surface roughness could lead to a significant decrease of eddy activity downstream and thereby limit the zonal extent of the storm track. It has also been suggested that orographically induced stationary waves could also modulate the eddy amplitudes, leading to localization of eddy activity and hence, limits to the zonal extent of a storm track. Obviously, zonal changes in baroclinicity due to land–sea contrast, while perhaps inadequate to fully explain the spatial extent of a storm track, certainly play an important role in determining its location. How these (or other) factors combine to limit the zonal extent of the storm track in the real atmosphere remains to be seen.

Acknowledgments. The authors would like to thank Dr. I. Held for valuable discussions, Mr. J. Sheldon, Dr. S. Garner, and the reviewers for editorial comments, Dr. N. C. Lau for assisting with the analyses of ECMWF data, and J. Varanyak and the GFDL drafting department for their assistance in preparing the figures. One of the authors (EC) is supported by NSF Grant ATM 8800667.

REFERENCES

Blackmon, M. L., 1976: A climatological spectral study of the 500-mb geopotential height of the Northern Hemisphere. *J. Atmos. Sci.*, **33,** 1607–1623.

——, Y. H. Lee, J. M. Wallace, and H. H. Hsu, 1984: Time variation of 500-mb height fluctuations with long, intermediate, and short time scales as deduced from lag-correlation statistics. *J. Atmos. Sci.*, **41,** 981–991.

Cai, M., and M. Mak, 1990: On the basic dynamics of regional cyclogenesis. *J. Atmos. Sci.*, **47,** 1417–1442.

Chang, E. K. M., 1993: Downstream development of baroclinic waves as inferred from regression analysis. *J. Atmos. Sci.*, **50,** in press.

Eady, E. T., 1949: Long waves and cyclone waves. *Tellus,* **1,** 33–52.

Farrell, B., 1982: Pulse asymptotics of the Charney baroclinic instability problem. *J. Atmos. Sci.*, **39,** 507–517.

Frederiksen, J. S., 1983: Disturbances and eddy fluxes in Northern Hemisphere flows: Instability of three-dimensional January and July flows. *J. Atmos. Sci.*, **40,** 836–855.

Gall, R., R. Blakeslee, and R. C. J. Somerville, 1979: Baroclinic instability and the selection of the zonal scale of the transient eddies of middle latitudes. *J. Atmos. Sci.*, **36,** 767–784.

Grotjahn, R., 1984: Baroclinic instability in a long wave environment. Part II: Ageostrophic energy conversions. *Quart. J. Roy. Meteor. Soc.*, **110,** 669–693.

Hoskins, B. J., and P. J. Valdes, 1990: On the existence of storm-tracks. *J. Atmos. Sci.*, **47,** 1854–1864.

Hovmöller, E., 1949: The trough-and-ridge diagram. *Tellus,* **1**(2), 62–66.

Joung, C. H., and M. H. Hitchman, 1982: On the role of successive downstream development in East Asian polar air outbreaks. *Mon. Wea. Rev.*, **110,** 1224–1237.

Lau, N. C., and J. M. Wallace, 1979: On the distribution of horizontal transport by transient eddies in the Northern Hemisphere wintertime circulation. *J. Atmos. Sci.*, **36,** 1844–1861.

Lee, S., 1991: Baroclinic wave packets in models and observations. Ph.D. dissertation, Princeton University, 214pp.

Lim, G. H., and J. M. Wallace, 1991: Structure and evolution of baroclinic waves as inferred from regression analysis. *J. Atmos. Sci.*, **48,** 1718–1732.

Manabe, S., and A. J. Broccoli, 1990: Mountains and arid climates of middle latitudes. *Science,* **247,** 192–195.

Merkine, L., 1977: Convective and absolute instability of baroclinic eddies. *Geophys. Astrophys. Fluid Dynamics,* **9,** 129–157.

Moura, A. D., and P. H. Stone, 1976: The effects of spherical geometry on baroclinic instability. *J. Atmos. Sci.*, **33,** 602–616.

Orlanski, I., and E. K. M. Chang, 1993: Ageostrophic geopotential fluxes in downstream and upstream development of baroclinic waves. *J. Atmos. Sci.*, **50,** 212–225.

——, and J. Katzfey, 1991: The life cycle of a cyclone wave in the Southern Hemisphere. *J. Atmos. Sci.*, **48,** 1972–1998.

Pierrehumbert, R. T., 1984: Local and global baroclinic instability of zonally varying flow. *J. Atmos. Sci.*, **41,** 2141–2162.

——, 1986: Spatially amplifying modes of the Charney baroclinic-instability problem. *J. Fluid Mech.*, **170,** 293–317.

Ross, B. B., and I. Orlanski, 1982: The evolution of an observed cold front. Part I: Numerical simulation. *J. Atmos. Sci.*, **39,** 296–327.

Simmons, A. J., and B. J. Hoskins, 1978: The life cycles of some nonlinear baroclinic waves. *J. Atmos. Sci.*, **35,** 414–432.

——, and ——, 1979: The downstream and upstream development of unstable baroclinic waves. *J. Atmos. Sci.*, **36,** 1239–1254.

——, and ——, 1980: Barotropic influences on the growth and decay of nonlinear baroclinic waves. *J. Atmos. Sci.*, **37,** 1679–1684.

Valdes, P. J., and B. J. Hoskins, 1988: Baroclinic instability of the zonally averaged flow with boundary-layer damping. *J. Atmos. Sci.*, **45,** 1584–1593.

Wallace, J. M., G. H. Lim, and M. L. Blackmon, 1988: Relationship between cyclone tracks, anticyclone tracks, and baroclinic waveguides. *J. Atmos. Sci.*, **45,** 439–462.